UC Davis
UC Davis Previously Published Works

Title

An overview of recent HL-2A experiments

Permalink

https://escholarship.org/uc/item/1sw9x42c

Journal

Nuclear Fusion, 53(10)

ISSN

0029-5515

Authors

Duan, XR
Ding, XT
Dong, JQ
et al.

Publication Date

2013-10-01

DOI

10.1088/0029-5515/53/10/104009

Peer reviewed

An overview of recent HL-2A experiments

X.R. Duan[1], X.T. Ding[1], J.Q. Dong[1], L.W. Yan[1], Yi Liu[1],Y. Huang[1], X.M. Song[1], X.L. Zou[2], M. Xu[1,3], Q.W. Yang[1], D.Q. Liu[1], J. Rao[1], W.M. Xuan[1], L.Y. Chen[1], W.C. Mao[1], Q.M.Wang[1], Z. Cao[1], B. Li[1], J.Y. Cao[1], G.J. Lei[1], J.H. Zhang[1], X.D. Li[1],W. Chen[1], K.J. Zhao[1], W.W. Xiao[1], C.Y. Chen[1], D.F. Kong[4], M. Isobe[5], S. Morita[5], J. Cheng[1], S.Y. Chen[4], C.H. Cui[1], Z.Y. Cui[1], W. Deng[1], Y.B. Dong[1], B.B. Feng[1], W.Y. Hong[1], M. Huang[1], X.Q. Ji[1], G.S. Li[1], H.J. Li[1], Qing Li[1], C.H. Liu[1], J.F. Peng[1], B.Z. Shi[1], Y.Q. Wang[1], L.H. Yao[1], L.Y. Yao[1], D.L. Yu[1], L.M. Yu[1], B.S. Yuan[1], J. Zhou[1], Y. Zhou[1], W.L. Zhong[1], G. Tynan[3], P. Diamond[3], C.X. Yu[4], Yong Liu[1]and the HL-2A Team

[1] Southwestern Institute of Physics, PO Box 432, Chengdu 610041,People's Republic of China

[2] CEA, IRFM, F-13108 Saint-Paul-lez-Durance, France

[3] Center for Momentum Transport and Flow Organization, University of California,San Diego, 9500 Gilman Drive, La Jolla, CA, 92093, USA

[4] Department of Modern Physics, University of Science and Technology of China,Hefei,People's Republic of China

[5] National Institute for Fusion Science, 322-6 Oroshi-cho, Toki-shi 509-5292, Japan

E-mail: duanxr@swip.ac.cn

Abstract

For the firsttime supersonic molecular beam injection (SMBI) and cluster jet injection (CJI) were applied to mitigate edge-localized modes (ELMs) in HL-2A successfully. The ELM frequency increased by a factor of 2-3 and the heat flux on the divertor target plates decreased by 50% on average after SMBI or CJI. Energetic particle induced modes were observed in different frequency ranges with high-power electron cyclotron resonance heating (ECRH). The high frequency (200-350kHz) of the modes with a relatively small amplitude was close to the gap frequency of the toroidicity-induced Alfven eigenmode. The coexistent multi-mode magnetic structures in the high temperature and low-collision plasma could affect the plasma transport dramatically. Long-lived saturated ideal magnetohydrodynamic instabilities during strong neutral beam injection heating could be suppressed by high-power ECRH. The absolute rate of nonlinear energy transfer between turbulence and zonal flows was measured and the secondary mode competition between low-frequency (LF) zonal flows (ZFs) and geodesic acoustic modes (GAMs) was identified, which demonstrated that ZFs played an important role in the L–H transition. The spontaneously generated $E \times B$shear flow was identified to be responsible for the generation of a large-scale coherent structure (LSCS), which provided unambiguous experimental evidence for the LSCS generation mechanism. New meso-scale electric potential fluctuations (MSEFs) at frequency $f \sim 10.5$ kHz with two components of $n = 0$ and $m/n = 6/2$were also identified in the edge plasmas for the first time. The MSEFs coexisted and interacted with magnetic islandsof $m/n = 6/2$, turbulence and LF ZFs.

1. Introduction

In recent years, the aim of the HL-2A tokamakprogramme has been to address key physics issues relevant to ITER experiments. In order to achieve the goal, many subsystems such as auxiliary heating and new diagnostic systems have been improved or developed. For example, the newly installed 2 MW/140 GHz ECH system makes the total electron cyclotron resonance heating (ECRH)/electron cyclotron current drive (ECCD) power up to 5MW. A far-infrared laser polarimeter for Faraday rotation measurements [1], a motional Stark effect system for magnetic field and current profile measurements, a fast electron radiation measurement system [2], etc have been developed. These systems significantly enhance the feasibility of studying advanced plasma physics subjects on the machine.

The achieved operation parameters on HL-2A (R = 1.65 m, a = 0.4m) are as follows: the toroidal magnetic field $B_t = 2.7\,T$, plasma current $I_p = 430kA$, discharge duration 6.1 s, line-averaged density $n_e = 6 \times 10^{19}\,cm^{-3}$, electron and ion temperatures $T_e = 5\,keV$ and $T_i = 2.8\,keV$, respectively. Since the last Fusion Energy Conference, the experiments on the HL-2A tokamak have been focused on the investigation of H-mode related physics, including edge-localized modes (ELM) mitigation and L–H transition mechanism, energetic particle (EP) physics and magnetohydrodynamic (MHD) instabilities, and L–H transition relevant turbulence and zonal flows (ZF), etc. In particular, the first demonstration of converting large ELMs into a series of small ELMs with supersonic molecular beam injection (SMBI) or cluster jet injection (CJI) [3, 4], the investigation of toroidicity-induced Alfven eigenmodes (TAEs) and beta-induced Alfven eigenmodes (BAEs) [5, 6], ELM-free H-mode and intermediate limit-cycle oscillation (LCO) (I-phase) [7, 8], nonlinear energy transfer [9, 10], blob generation and its dynamics [11], meso-scale electric fluctuations and turbulence interactions [12] have significantly contributed to the understanding of the underlying physics. The major experimental results are reviewed in this paper while details are described in the corresponding references. This paper is arranged as follows. The results on ELM mitigation by SMBI and CJI are given in section 2. The investigation of EP physics in ohmic and high ECRH power plasmas is introduced in section 3. Studies on turbulence and transport, including nonlinear energy transfer, interaction among turbulence, magnetic islands and ZFs, etc, are presented in section 4. Section 5 is devoted to a brief summary and near future plans.

2. ELM mitigation by SMBI and CJI

The basic planned operational regime for ITER is theELMyH-mode, which is feasible for long-pulse discharges of advanced tokamak plasmas [13]. On the other hand, however, large ELMs may lead to strong heat loads on the divertor target plates, and result in significant erosion or even damage of the plates. Hence, it is very important to develop tools to mitigate or control the ELMs. In recent years, some techniques have been proposed and applied to mitigate ELMs, such as nitrogen seeding injection [14], pellet pacing [15], resonant magnetic perturbation (RMP) [16] and other external perturbation fields [17]. Pellet pacing was demonstrated on ASDEX Upgrade for the

first time. The large intrinsic ELMs at 3Hz were completely replaced by regular, pellet-induced type-I ELMs at 19 Hz with the same frequency as the pellets. The latter was triggered less than 0.2 ms after pellet arrival at the plasma edge with a velocity of 560ms^{-1}. Recently, high-frequency pellet pacing in DIII-D has been found to considerably reduce the target ELM intensity and core impurity accumulation simultaneously when applied at rates 10 times higher than the natural ELM frequencies [18]. The ELMs were triggered well before the pellet of speed less than 200ms^{-1} reaches the pedestal top, implying that even smaller pellets can be used. The ELITE calculation indicates that the pedestal conditions of pellet pacing are far from the boundary for peeling and ballooning stability, and a narrower pedestal width is observed before the width expands to the critical width at which the natural ELM occurs.
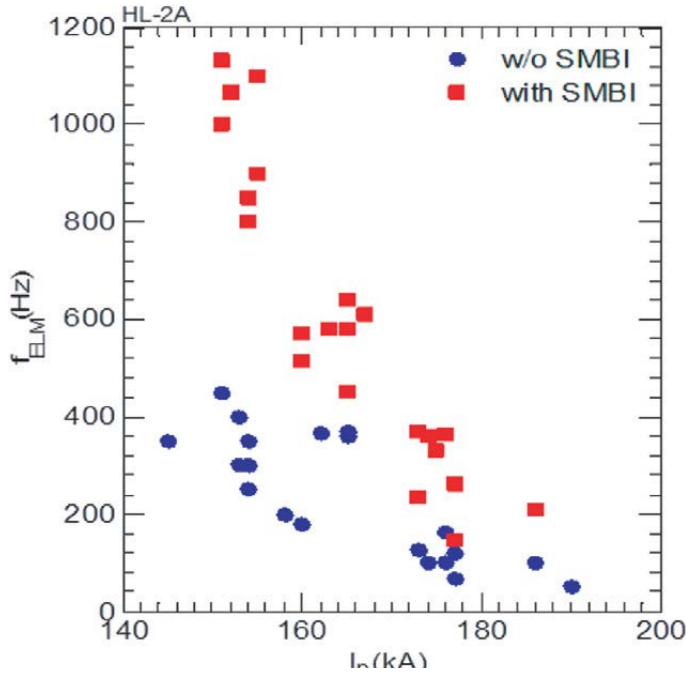

Figure 1. The ELM frequency versus plasma current for cases with (red squares) and without (blue circles) SMBI.

Since the ELMy H-mode was achieved on HL-2A in 2009 and it was later found that the SMBI was beneficial for triggering the L–H transition [19], the HL-2A team has been proposing to mitigate ELMs with the use of SMBI. One of the major motivations of the experiments is to explore the possibility for ELM mitigation with SMBI/CJI, which is much simpler and cheaper than pellet injection and RMP. ELM mitigation with SMBI was first demonstrated successfully in 2010 [3, 4, 20]. Figure 1 shows a comparison of the ELM frequency with and without SMBI at different plasma currents. The ELM frequency with SMBI (f_{ELM}^{SMBI}) is higher than the frequency without SMBI (f_{ELM}^0), while the intensity of the former is much less than the latter. The frequency ratio (f_{ELM}^{SMBI}/f_{ELM}^0) is about 2–3.5. For these discharges, the auxiliary heating power is about 0.9–1.4MW, the safety factor is $q_{95} = 2.9 - 3.5$ and $\langle n_e \rangle$ is about $(1.8 - 2.3) \times 10^{19} m^{-3}$.

In the experiment it was found that, if the backing gas of the SMBI system was cooled with liquid nitrogen, clusters (similar to micro-pellets) could be formed in the supersonic molecular beam under some conditions such as high pressures. The cooled SMBI could penetrate deeper than the normal SMB into the plasma, and was named CJI. It is expected to be more efficient for ELM mitigation due to deeper penetration into the pedestal. Figure 2 shows a typical discharge for ELM mitigation with CJI. From the top to the bottom of the figure are (a) the D_α emission intensity in the divertor chamber, where the blue pulse indicates the control signal for the CJI system, (b) the thermal radiation intensity in the divertor chamber, where τ indicates the influence time of ELM mitigation by CJI, which is about 30 ms, (c) the ELM frequency calculated from the time interval between adjacent ELMs, where f_{ave}^0 and f_{ave}^{CJI} represent the averaged ELM frequencies before and immediately after (in the duration of τ) CJI, respectively, with $f_{ave}^{CJI}/f_{ave}^0 = 2.24$, (d) the intensity of the ELMs, where I_{ave}^0 and I_{ave}^{CJI} are the averaged radiation intensities before and immediately after (in the duration of τ) CJI, respectively, with $I_{ave}^{CJI}/I_{ave}^0 = 0.38$, (e) the stored energy, which does not change significantly after CJI, i.e. the plasma confinement is not degraded during the process, while the thermal radiation intensity due to ELM bursts decreases obviously, as seen from figure 2(b).
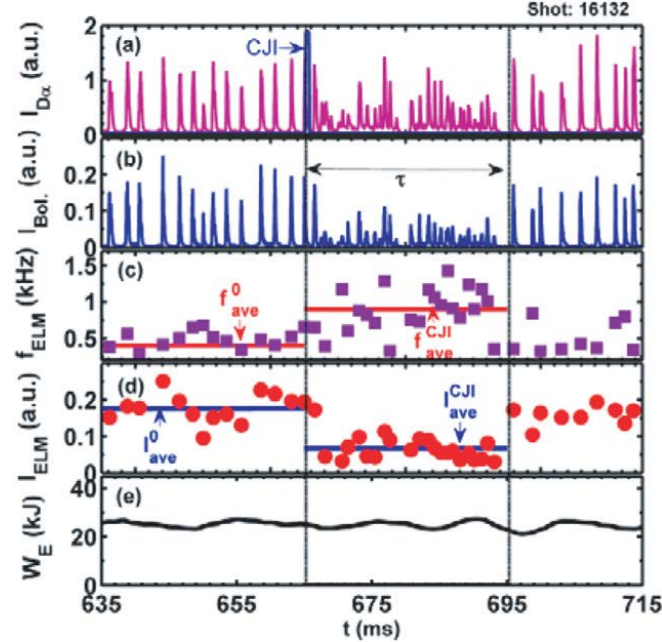

Figure 2. The ELM mitigation using CJI. (a) D_α in the divertor chamber, (b) the intensity of thermal radiation in the divertor chamber, (c) ELM frequency, (d) ELM intensity, (e) the stored energy.
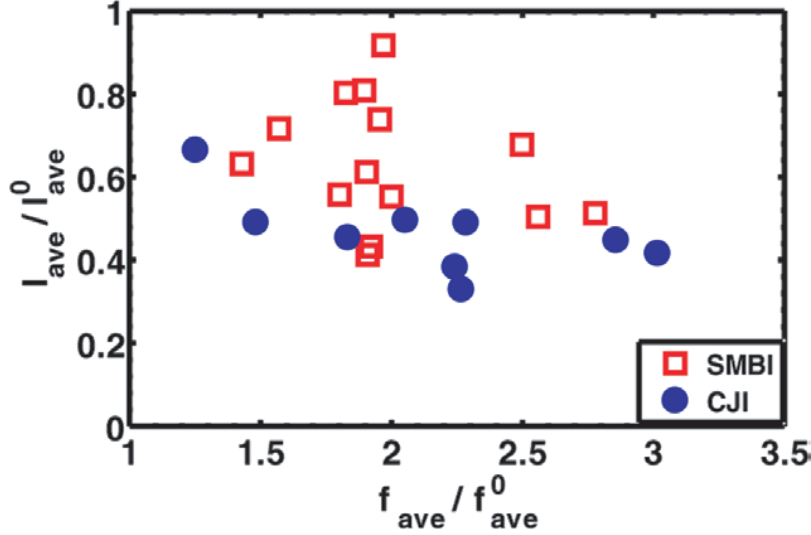
Figure 3. The comparison of ELM mitigation effects between SMBI and CJI.

Figure 3 presents a comparison of the ELM mitigation effect between the SMBI and the CJI. The results indicate that the relative intensity (intensity reduction factor) of the ELMs with CJI mitigation is clearly lower than that with SMBI for the same relative frequency (frequency enhancement ratio).

The major goal of ELM mitigation is to reduce the heat load on the divertor target plates. In the experiments with CJI, it is found that the heat flux on the target plates after CJI decreases dramatically. Figure 4 shows the details of the result. Given in figure 4(a) are the control signals of the CJI system. Figure 4(b) shows the D_α emission intensity in the divertor chamber. It clearly indicates that the ELM burst frequency increases obviously after CJI and the increase can last for about 30–40 ms (mitigation time scale). Shown in figure 4(c) is the line-averaged electron density, which has a slight rise ($\Delta n_{el}/n_{el}$ is about 5%) after a CJI pulse. Figure 4(d) gives the stored energy, which remains almost unchanged after a CJI ($\Delta W_E/W_E$ is about 7%), indicating that the CJI does not degrade the plasma high confinement obviously. Figure 4(e) represents the heat flux at the outer divertor target plate, estimated with the formula $q_{div} \sim \gamma C_s n_{et} T_{et} sin\theta$, where $\gamma \sim 7$ is the sheath heat transmission factor, C_s is the ion sound speed, $\theta \sim 2^\circ - 3^\circ$ is the incident angle, T_{et} and n_{et} are the electron temperature and density, respectively, at the target plate measured by Langmuir probes, Z denotes the vertical position on the target plate, localized 81 cm below the midplane. The results showthat the divertor heat flux has an abrupt drop after each CJI, and then maintains a lower value for about 30–40 ms. On average, the heat flux in the mitigation period after a CJI is about 50% of that before a CJI.
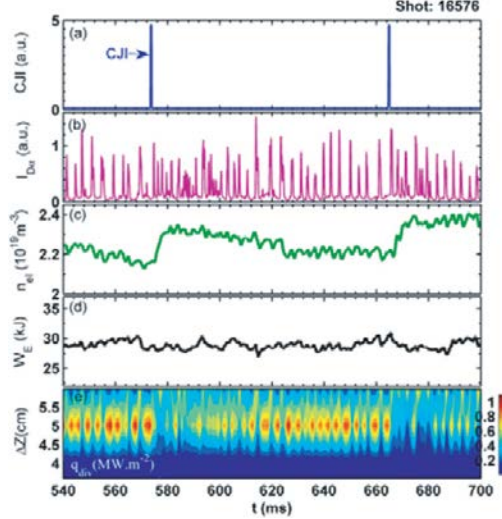
Figure 4. The ELM mitigation using CJI. (a) The control signal of CJI, (b) D_α in the divertor chamber, (c) line-averaged electron density, (d) stored energy, (e) heat flux at the outer target plate.

ELM mitigations with SMBI were also performed successfully in the recent experimental campaigns on EAST [22] and KSTAR [21], and the above-mentioned results from HL-2A are all confirmed. In addition, the results on EAST and KSTAR show that the ELM mitigation with SMBI is more efficient, for example, lasting a longer period of time after an SMBI pulse, for type-I ELMy H-mode than for type-III ELMy H-mode, indicating the possibility of application to ELM mitigation on ITER although a more detailed investigation is urgently needed. The physics mechanisms for ELM mitigation with SMBI/CJI are under intensive investigation and primary progress has been made recently [23]. The basic mechanism of mitigation is the triggering of small-scale pedestal avalanches by additional grain injection directly into the H-mode pedestal. The small-scale avalanches prevent the gradients from building-up to marginality throughout the pedestal and, thus, avoid large-scale transport events which span the full extent of that region. The SMBI deposition just inside the separatrix seems sufficient to trigger small transport events and hence to prevent large ELMs. According to the simple sand-pile model, it is shown that shallow particle deposition can induce frequent small particle ejection and prevent formation of large crashes [23]. For deep particle deposition, mitigation of large crashes is rarely observed. The experimental results on ELM mitigation by SMBI/CJI in HL-2A are qualitatively in consistence with the prediction of the sand-pile model.

3. EP physics

Alfvenic and acoustic modes are very important physics phenomena in burning plasmas, such as ITER and DEMO. These instabilities can be excited by EPs produced by radio frequency (RF) or neutral beam injection (NBI) heating and fusion reactions [24–26]. Associated nonlinear wave–particle interactions can significantly enhance EP transport, which would degrade the overall plasma confinement and

damage plasma-facing components of fusion devices. Important and interesting subjects in the field include observation and investigation of generation mechanisms of the fluctuations, processes that govern the energy/particle flux evolution, and roles of nonlinear wave–particle and wave–wave interactions in energy transition and plasma confinement.

Fishbone instabilities and BAE were identified and investigated in the previous experiments on HL-2A [5, 27, 28]. Recently, new experimental phenomena, e.g. coexistence of multi-Alfvenic modes [6] induced by energetic electrons and the frequency jump of electron fishbone (e-fishbone) modes [29] during high-power ECRH, have been observed. These new results may contribute to the understanding of the underlying physics mechanism for the excitation of the low-frequency (LF) Alfvenic and acoustic fluctuations.

3.1. Coexistence of multi-e-BAE modes

The multi-LF Alfvenic modes induced by energetic electrons have been observed during high-power ECRH heating. Given in figure 5 are the evolutions of (a) the plasma current, (b) line-averaged electron density (n_e), (c) electron temperature (T_e) from electron cyclotron emission (ECE), (d) hard x-ray (HXR) radiation in the energy range 10–20 keV, (e) signals of Mirnov probes, (f) ECRH power and (g) the frequency spectrum of Mirnov signals in shot 17461. The evolutions of the magnetic fluctuations observed with the Mirnov coils and soft x-ray (SXR) arrays show that two or three modes appear during the high-power ECRH with off-axis deposition (but still inside the q = 1 flux surface). From figure 5 it can be seen that the intensity of ECE increases with the ECRH power and the value of ne decreases first, and then remains invariant. The HXR radiation, induced by the energetic electrons, increases with the ECRH power dramatically. The evolution of the frequency spectrum of the magnetic fluctuations (figure 5(g)) indicates that the frequency spectra change dramatically with increase in the ECRH power. When the ECRH power is lower than 600kW, one peak around 22 kHz can be clearly seen only in the frequency spectrum, which has been identified as e-BAE [28]. When the power is higher than about 600kW, two or three peaks appear. In addition, the spectrum becomes wide when the power is higher than 1.5MW. After ECRH is switched off, the spectrum resumes to the previous one with one frequency peak only. The modes are located in the region outside the half-normalized minor radius and proved to be related to the energetic electrons strongly.
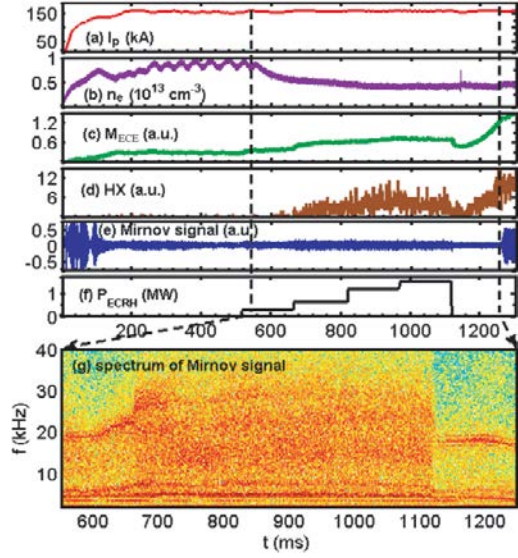
Figure 5. Evolutions of (a) the plasma current, (b) the line-averaged electron density, (c) electron temperature from ECE, (d) hard x-ray (HXR) in the energy range of 10–20 keV, (e) the signals of Mirnov probes; (f) the ECRH power, (g) the frequency spectrum of Mirnov signals in shot 17461.
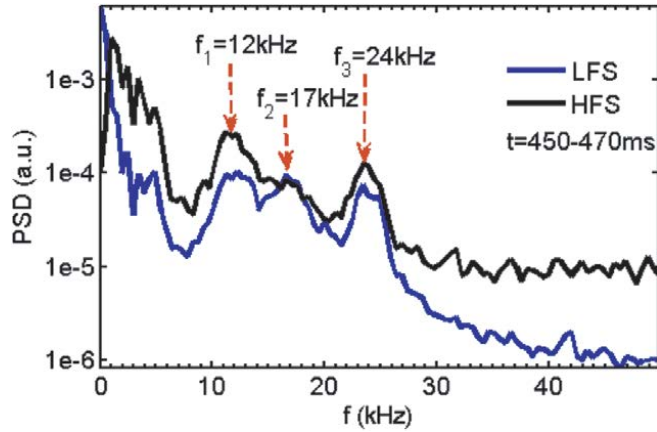

Figure 6. The poloidal power density spectrum of the magnetic fluctuations measured by Mirnov probes in shot 17929 with 1.36MW ECRH.

To obtain more detailed features of the modes during highpower heating, the power density spectra and both the toroidal and poloidal mode numbers were analysed and the results are given in figure 6. Three peaks at frequencies 12 kHz, 17 kHz and 24 kHz are found in the power density spectra, which are denoted as f_1, f_2 and f_3 in figure 6. The mode numbers of the three modes are estimated to be m/n = 4/1, 5/2 and 2/1, respectively, using a global fit of the phase of the Mirnov signal.

The parameter dependence of the mode frequencies is investigated by means of a statistical data analysis. The results show that the frequencies of the three modes decrease with the plasma density, while the frequencies of the modes increase with the toroidal magnetic field at the same density. As we know, the Alfven velocity is proportional to $Bn_e^{-1/2}$, where B is the magnetic field and n_e is the plasma density,

so the frequencies increase with the Alfven velocity, indicating that the magnetic fluctuations are related to Alfvenic modes. According to the available theory about the BAE, the frequency of the BAE is also related to ion and electron temperatures, as shown in the formula $f_{BAE} \sim (7/4 + T_e/T_i)^{1/2} T_i^{1/2}$ [30]. A statistical analysis shows that the ion temperature measured by neutral particle analysis (NPA) changes slightly in low-density ECRH plasma. It was found that the frequencies of the three modes tend to increase with $(7/4 + T_e/T_i)^{1/2} T_i^{1/2}$. Hence the frequencies of the observed modes seem to be in agreement with this relation qualitatively.

3.2. Frequency jump of e-fishbone mode

The fishbone modewas experimentally observed duringECRH on the HL-2A.With increasing of the ECRH power, the mode frequency showed some new phenomena with up- and down-chirping behaviour, sometimes with V-font-style sweeping. The chirping mode during ECRH has also been identified as the fishbone instability induced by energetic electrons in the previous investigation on other devices [5, 28]. The frequency jump phenomena have been observed during LHCD in Tore Supra [31, 32] and the distributions of the energetic electrons have been obtained by the multi-channel HXR. A frequency jump means the frequency changes quickly within several tens of microseconds. It is worth pointing out that the resultspresented here are different from the e-fishbone frequency jump observed during LHCD, because the trapped particles are dominant here in ECRH plasmas of HL-2A, while passing electrons may dominate in LHCD plasmas of Tore Supra.

Periodic mode frequency jumps are detected by an SXR array during high-power ECRH on HL-2A. The e-fishbone mode frequency jumps are observed when the power is deposited on the magnetic axis in plasmas at low electron densities. Presented in figure 7 are the temporal evolutions of the plasma current, line-averaged electron density, electron temperature from ECE, HXR in the energy range 10–20 keV, the signal of Mirnov probe, ECRH power and the frequency spectrum of signals of Mirnov coils in shot 17829. In order to investigate the e-fishbone behaviour for different ECRH powers, the power is increased from 0.3 to 1.15MW in four steps (0.3 MW/0.57 MW/0.89 MW/1.15MW) from 1.02 to 1.42 s. Other discharge parameters are plasma current $I_p = 155kA$ and toroidal magnetic field $B_t = 1.22T$. Because of the pump-out effect, the electron density decreases from 1.3×10^{19} to $0.4 \times 10^{19} m^{-3}$during ECRH, as shown in figure 7(a). The frequency spectra of the SXR show that the frequency of the fluctuations is about 5 kHz in the lowpower phase, and increases to about 8 kHz when the ECRH power increases to 1.2MW. The ECE and HXR emissions shown in figures 7(b) and (c) indicate that the number of energetic electrons increases dramatically when the ECRH power increases. The frequency jumps can be observed vaguely, when the ECRH power increases to about 0.6MW. It can be clearly seen that the frequency jumps between 8 and 13 kHz when the power is about 1.2MW, as shown in figure 7(d).

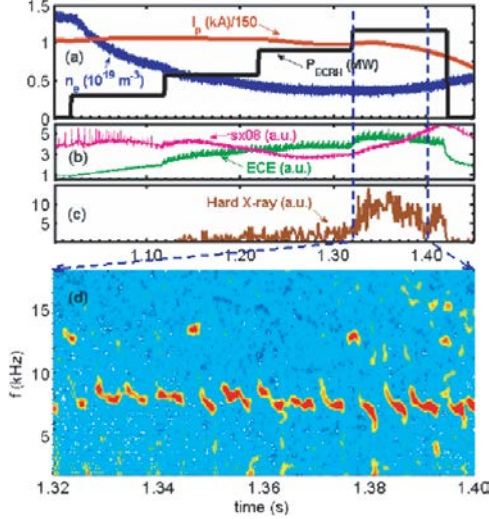**Figure 7.** Temporal evolution of (a) plasma current, line-averaged electron density, and ECRH power, (b) electron temperature from ECE and soft x-ray intensity, (c) hard x-ray with the energy of 0–20 keV and (d) soft x-ray frequency spectra in shot 17892.

The poloidal and toroidal mode numbers for the low- and high-frequency branches are m/n = 1/1 and 2/2, respectively. In order to find the relationship between ECRH power and e-fishbone frequency of low- and high-frequency branches, a statistical analysis is carried out, with plasma current and the line-averaged electron density in the ranges 155–160 kA and $(0.4 - 0.7) \times 10^{19} m^{-3}$, respectively, the toroidal magnetic field $B_t = 1.2 - 1.22T$, for which the ECRH power is deposited inside the q = 1 surface. It is observed that the threshold ECRH powers for the appearance of low- and high-frequency e-fishbone modes are about 0.6MWand 0.9MW, respectively, and not only the frequency of the LF branch (the blue circles) but also that of the high-frequency branch (the red diamonds) increases with the ECRH power, as shown in figure 8. By other statistics about the relationship between the deposition position of ECRH power and the appearance of frequency jumps, it is also found that the frequency jumps appear only when highpower ECRH is deposited inside the q = 1 surface.

3.3. Long-lived mode instabilities

A long-lived mode (LLM), observed [33] during NBI with weakly reversed or broad low magnetic shear [34, 35], is considered as a pressure-gradient-driven MHD mode. It often results in rotation flattening in the core plasma and degrades fast-ion confinement. In HL-2A plasmas, an n = 1 long-lived saturated mode and its higher toroidal mode number harmonics were frequently observed during the NBI heating phase with a flat core safety factor profile, as shown in figure 9. In the resulting low shear region around the q = 1 surface, the stabilizing effect of magnetic field line bending becomes less important and the pressure gradient will be able to destabilize ideal modes resonant with the magnetic field in the core. This mode can persist for

10–400 ms or longer with a frequency in the range 10–20 kHz. In the presence of LLM, reductions in the electron density and the plasma stored energy, as well as fast ion losses are usually observed.

Studies have also shown that the LLM can be suppressed by ECRH which may modify the q profile in the plasma core. The experimental results shown in figure 9 indicate that the higher the toroidal mode number n, the easier the harmonics can be suppressed by increased ECRH power.
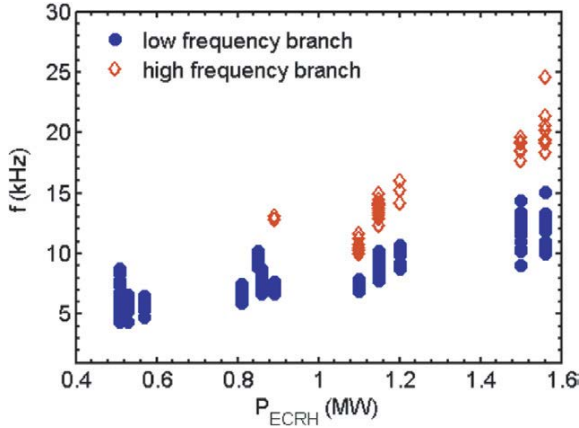

Figure 8. Relationship between ECRH power and e-fishbone mode frequency of low- and high-frequency branches. The blue circles and red diamonds are for the low- and high-frequency branch e-fishbone modes, respectively.
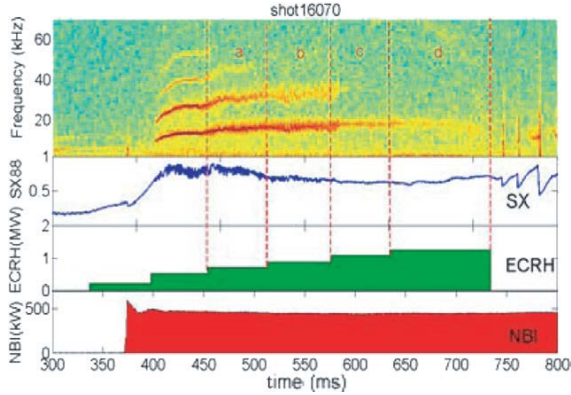

Figure 9. Fourier spectrogram of soft x-ray signal showing the long-lived mode during NBI on HL-2A. Higher-n modes are suppressed by increased ECRH power.

4. Transport and turbulence

Turbulence dynamics and the associated particle, momentum and heat transports across the magnetic field in tokamak edge plasmas are among the most important research topics as they largely determine the fusion plasma confinement and are critical for realizing and maintaining the high-confinement operation regime (H-mode) of magnetic confinement fusion devices. In the past few years, significant progress has been made in the HL-2A tokamak in understanding the turbulence and shear flow interactions, MSEFs and its interaction with magnetic island and turbulence, blobs

and their generation mechanism, as well as the intermediate oscillatory phase during L–H transitions. These experimental results significantly contribute to the understanding of edge turbulence and transport phenomena, and the L–H transition mechanism.
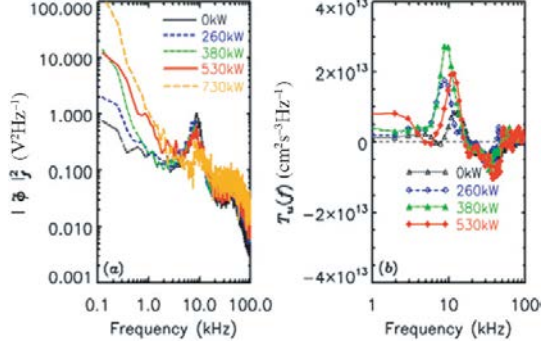

Figure 10. At different ECRH power (a) frequency spectrum of potential fluctuations (b) nonlinear kinetic energy transfer rate $T_v(f) = -Re \sum_{f_1} \langle \vec{v}^*_{\perp f} \cdot (\vec{v}_{f-f_1} \cdot \nabla_\perp v_{\perp f_1}) \rangle$.

4.1. Frequency-domain nonlinear energy transfer and its real-space counterpart

The absolute rate of nonlinear energy transfer among broadband turbulence, LF ZFs and geodesic acoustic modes (GAMs) [36, 37] was measured for the first time in tokamak plasmas using two independent methods across a range of heating powers (figure 10(b)) [9]. A frequency-domain bispectral method was used to determine the energy transfer rate among fluctuations at different frequencies. This method is an experimental evaluation of the quadratic nonlinear term in the ion momentum equation and can give the rate of energy transfer as well as its direction during nonlinear coupling processes. Details about this method can be found in [38, 39]. At a particular frequency, a negative energy transfer rate means that the fluctuation at this frequency loses energy through nonlinear interactions, while a positive value means that the fluctuation at this frequency gains energy. In figure 10(b), the energy transfer rates at typical turbulence frequencies 20– 80 kHz are all negative, and the energy transfers at both GAMs and ZF frequencies (also at higher frequencies>80 kHz) are all positive. Combined with the two-dimensional energy transfer [9], it is clear that turbulent kinetic energy from intermediate frequencies (20–80 kHz) is transferred into ZFs and GAMs, as well as into fluctuations at higher frequencies (>80 kHz). This result is consistent with the potential autopower spectra in figure 10(a), which indicates that much stronger (by a factor of more than 100) LF fluctuations, including ZFs and LF components of the ambient turbulence of small scales, develop as the plasma heating power is increased from 0 to 730kW. Note that the autopower spectrum at low frequencies also includes the contribution from LF turbulent fluctuations. The cross-power spectrum between two channels that lie on the same flux surface and are with long-distant poloidal separation would better represent the ZF intensity [40], but unfortunately it is not available for this experiment.
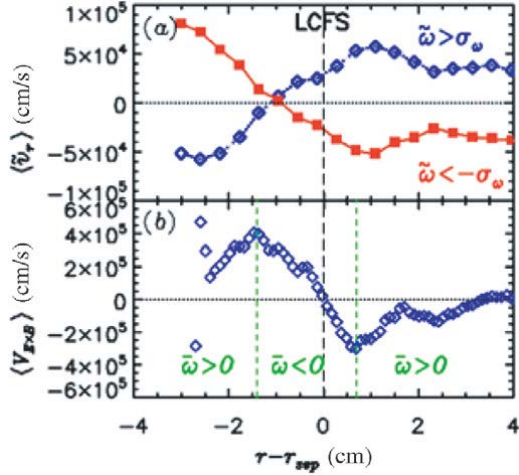
Figure 11. (a) Radial velocity profiles for positive and negative eddies/blobs estimated by using conditional average with vorticity as the trigger reference. (b) Mean $E \times B$ flow velocity and its associated mean vorticity.

Using conditional average, the turbulence drive for ZFs was found to be associated with negative vortices that carry excessive positive (electron diamagnetic direction) momentum and concentrate at around last closed flux surface (LCFS), and those positive vortices that have a deficit of positive momentum and diverge from around the LCFS (figure 11). This immediately means that turbulent vortices accumulate excessive positive momentum around the LCFS, and points naturally towards a picture in which turbulence acts to amplify or reinforce the equilibrium shear flow that exists around the LCFS. Notice that the propagation of the vortices, i.e. the vorticity flux, is actually related to the Reynolds force through the Taylor identity and could be written as $\langle \tilde{v}_r \tilde{\omega} \rangle = \langle \tilde{v}_r \nabla_\perp^2 \tilde{\phi} \rangle \approx \partial \langle \tilde{v}_r \tilde{v}_\theta \rangle / \partial r = -F^\theta_{Reynol\,ds}$. As the heating power increases, the vortices concentrate turbulent momentum in the shear region more efficiently as compared with when the heating is lower, leading to a larger Reynolds force at a higher heating power (not shown here due to space limit). Therefore, these results provide a clear picture of the essential physics that leads to a bifurcation in the turbulence and shear flow. Also since the vortcity drive gets stronger as the heating power is increased, it should naturally lead to a very strong shear flow that can suppress the turbulent transport and ultimately lead to H-mode with sufficient heating.

4.2. Synchronization of GAMs and magnetic islands

Turbulence, flow and magnetic island are three factors playing important roles in the confinement of magnetic fusion plasmas and have been under intensive investigation for decades. Recent works have shown that magnetic islands developed around a rational resonant surface (RRS) contribute to shear flow and quasi-coherent mode formation and that turbulence modulation is amplified in the same region [41, 42]. It

13

is also predicted that magnetic islands are inevitable in tokamak plasmas and coexist with meso-scale fluctuations and turbulence [43]. However, MSEFs resulting from the synchronization of GAMs and magnetic islands have not been observed in experiments.
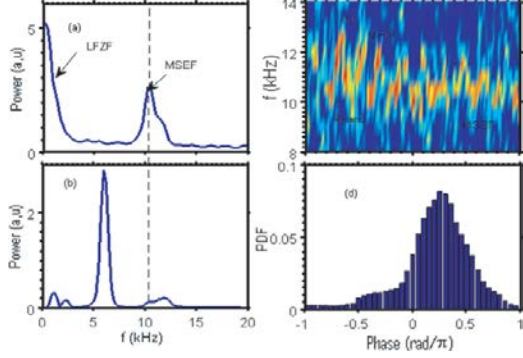

Figure 12. The auto-power spectra of the floating potential (a) and magnetic fluctuations (b), the time evolutions of electric fluctuations (t = 560–620 ms) (c) the probability distribution of the phase shifts between MSEFs and magnetic islands (d).

NewMSEFs at~10.5 kHz coexisting and interacting withmagnetic islands are identified in the edge plasmas of theHL-2A tokamak for the first time. The analysis of the measuredelectric potential fluctuations shown in figure 12(a) indicatesthat there are two components of n = 0 and m/n = 6/2,coexisting at the MSEF frequency. Here, m and n arethe poloidal and toroidal mode numbers, respectively. Twocomponents of n = 0 and m/n = 6/2 magnetic fluctuationsat the frequency of 10.5 kHz are also detected and the latteris identified as a tearing mode (figure 12(b)). The MSEFs,peaking in the region near the RRS of safety factor q = 3, arefound to be well correlated with the magnetic fluctuations of10.5 kHz. In addition, the peak at the frequency of 6 kHz isthe m/n = 3/1 tearing mode in the magnetic fluctuations.

The time evolutions of electric potential fluctuations in the frequency band of 8–14 kHz are given in figure 12(c). GAM with a frequency of~12.5 kHz and island potential fluctuations at the frequency ~10.5 kHz are observed from 560 to 590 ms. The GAM frequency decreases slowly while the frequency for the island potential fluctuations does not vary and is equal to that of the magnetic island of the m/n = 6/2 tearing mode. After ~590 ms, the GAM frequency reaches ~10.5 kHz and matches well with that of the m/n = 6/2 magnetic islands, and MSEFs are detected. The result suggests that the m/n = 6/2 magnetic islands entrain the GAM frequency. The phase shifts of the MSEFs are also locked at ~$\pi/4$, as shown in figure 12(d). The synchronization can be broken by sawteeth, but rapidly recovers.

4.3. Generation of large-scale coherent structure in edge plasmas

Large-scale coherent structures (LSCSs), or blobs (in OH or L-mode) stretching along magnetic field lines carry particle and heat flux across the field to the first wall in the scrape-off layer (SOL). Studying the LSCS formation mechanism is crucial for

reducing cross-field transport [44–46]. In this section, we report the experimental study of LSCS generation mechanism in HL-2A edge plasmas with a combination of an arc-shaped poloidal ten-tip array and a radial eight-tip array [11]. For a given plasma current I_p and a toroidal magnetic field B_t, a field line passing one tip of the arc-shaped poloidal ten-tip array may intersect one tip in the radial eight-tip array. Based on the significant correlation of the two tips along the same magnetic field line, we can reconstruct the LSCS propagation process [11]. Figure 13 shows the two-dimensional images of conditional average of the floating potentials at six time slices ($\Delta \tau = -8$ to $+2 \mu s$) with an adjacent interval of 2 µs. $\Delta r = 0$mm denotes the LCFS with an error of about 5 mm. It is clearly shown in figure 13(a) that a tilted turbulence structure with a spatial size of about 15–20mminitially appears and then grows in the observation region. The amplitude continues to grow and then forms two small islands, as seen in figures 13(b) and (c), which is the initial component of the LSCS. After that, the amplitudes of the two islands continuously increase and then they split into two circle structures (typical characteristics of blobs), see figure 13(e). Afterwards, the formed LSCS has apparent poloidal and radial movements with speeds of $1.2 - 2.0$ km$s^{-1}$and$0.5 - 0.8$ kms^{-1}, respectively. The radial velocity is about 1% of the local ion sound speed Cs. The ion gyroradius is estimated to be about 0.5 mm, which accounts for 2.5% of the size of the LSCS. These estimations are consistent with theoretical predictions of LSCS velocity and size [47]. This result is similar to that observed in theW-7 stellarator [48]. The spatiotemporal evolution of equilibrium E×B shear flow shows that there is a peak at $\Delta \tau = -4 \sim 0$ µs and in the layer 6–8mm inside the LCFS, where the eddy is split as described above. This observation suggests that LSCS generation is closely correlated with the strong sheared flow. The mean-flow shared time is estimated to be $\tau_{sh} = (k_\theta L_r \gamma_E / 2\pi)^{-1} = 8 \mu s$, where $L_r \sim 1.2 cm$, $k_\theta \sim 2.2 cm^{-1}$,$\gamma_E = 2.9 \times 10^5 s^{-1}$, which is close to the blob generation time $\tau_b \sim 6 - 8 \mu s$. On the other hand, the shearing rate of GAM flow peaks in the same layer with amplitude about 28% of the mean flow shearing rate and, therefore, does not play a dominant role in the LSCS generation. The comparison indicates that LSCS is virtually sheared off by the spontaneously generated E × B flow. In addition, bi-coherence analyses also suggest that the large-scale structure could be generated from the nonlinear three-wave coupling or inverse cascade of the ambient turbulence.
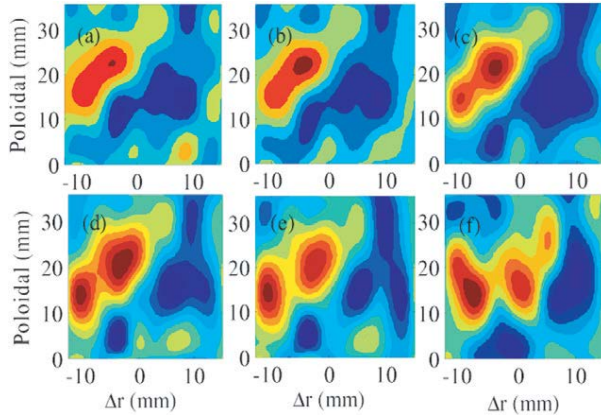
Figure 13. Two-dimensional images of conditional average of the floating potentials across the LCFS at six time slices with a 2 μs interval ($\Delta\tau = -8 \sim +2$ μs).
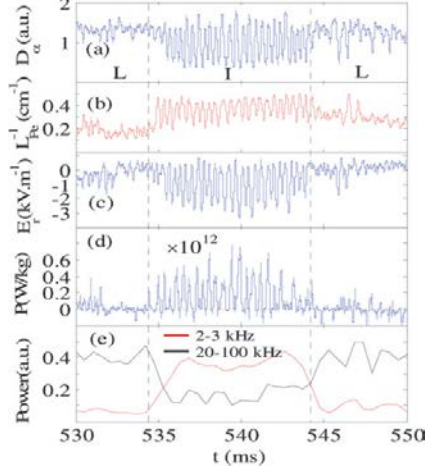

Figure 14. Time evolution of D_α (a), inverse scale length of electron pressure gradient (b), radial electrostatic field (c), energy transfer rate (d) and comparison of power for low frequency oscillation (2–3 kHz) and turbulence (20–100 kHz) (e).

4.4. Evolution of LF E × B oscillations in L–I–L transition

The study of LCO is crucial since LCO can regulate turbulent transport and potentially be the trigger for L–H transitions. Recently, L–I–L transition has been observed using a four-step Langmuir probe array in pure NBI-heated plasmas in the HL-2A tokamak ($P_{NBI} = 0.9 = 1.0\ MW$). The edge electron pressure gradient (at r−a = −3 mm) is estimated as $\partial P_e/\partial r = (P_{e1} - P_{e2})/\Delta r$, where P_{e1}, P_{e2} denote the local electron pressures with radial separation $\Delta r \sim 3$ mm. The radial electric field E_r is directly estimated using $E_r = -\partial V_P/\partial r$, where $V_P = V_f + \alpha T_e$ ($\alpha = 2.8$ for deuterium plasma) denotes the plasma potential. Figures 14(a)–(e) show the time evolutions of D_α emission, inverse of the scale length of electron pressure gradient, radial electric field (E×B shear flow), energy transfer rate between turbulence and LF E × B flows, and power contained in turbulence (20–100 kHz) and LF flows (2–3 kHz) during L–I–L transitions, respectively. The energy transfer rate is estimated as $P = R_s\langle\partial V_E/\partial r\rangle$, where $R_s = \langle\delta V_r \delta V_\theta\rangle$ is the Reynolds stress resulted from the tilting of turbulent structures by flowshear $\partial V_E/\partial r$. P is the Reynolds work exerted on shear flow by wave stress [9, 49]. As seen in figures 14(b) and (c), the L–I transition occurs at t = 534 ms when both the averaged radial electric field and the averaged electron pressure gradient start to rise. In figure 14(d), a positive value means that the energy is transferred from turbulence into LF shear flows (<5.0 kHz), and vice versa. It was found that the energy transfer rate is small but finite (mostly positive) during L-mode, rises sharply around the L–I transition, and is modulated violently by the 2–3 kHz oscillations during the I-phase. The relatively larger energy transfer rate during the I-phase is consistent with figure 14(e), where we can see an increase in the power associated with LF oscillations and a decrease in the power associated with turbulence.

The electron pressure gradient oscillates with the LF E × B flow during the I-phase (figures 14(b) and (c)). No strong mean flow developed for this shot, as we can see from the trend of electron pressure gradient in figure 14(b), the plasma fell back into L-mode. This observation indicates that strong mean flowmay be needed to trigger the confinement to the H-mode level [50, 51]. In cases when strong mean flow was observed to develop during the I-phase the plasma entered H-mode after the LCO phase. Detailed experimental evidence to support this speculation will be presented in a separate paper [8].

5. Summary and future plans

SMBI and CJI were successfully applied to mitigate ELM on HL-2A; the frequency of ELMs increased obviously after SMBI/CJI, and the heat flux to the divertor target plates decreased dramatically (by ∼50%) at the same time. The results of ELM mitigation by SMBI were also confirmed in the recent experiments on KSTAR [21] and EAST [22]. During the high-power ECRH, coexistence of multi-Alfvenic modes and e-fishbone frequency jump induced by energetic electrons were investigated; the GAM during strong TM in ohmic plasma induced by energetic electrons was identified. The generation mechanisms of these modes are under investigation. In addition, the long-lived saturated internal mode [33] and the beta-induced Alfven acoustic eigenmode (BAAE) in the range 15–40 kHz triggered by energetic ions produced by NBI heating with a power of 1MW were studied. Progress in understanding the turbulence and shear flow interactions, meso-scale electric fluctuation and its interaction with magnetic island, as well as the intermediate oscillatory phase during L–H transitions, has been made. Within the next few years, auxiliary heating systems, such as 3MW NBI and 2MW LHCD systems, are to be commissioned, and advanced diagnostic systems will be applied on HL-2A. The improvement and development of those hardware on HL-2A will enhance the ability for fusion science study and make important contributions to the establishment of ITER physics bases such as H-mode operation and energetic particle confinement.

Acknowledgments

References

[1] Zhou Y. *et al* 2012 *J. Instrum.* **7** C06012
[2] Zhang Y.P. *et al* 2010 *Rev. Sci. Instrum.* **81** 103501

[3] Xiao W.W. *et al* 2012 *Nucl. Fusion* **52** 114027

[4] Chen C.Y. *et al* 2012 *Proc. 24th Fusion Energy Conf. (San Diego, CA, 2012)* (Vienna: IAEA)EX/6-3Rb

www-naweb.iaea.org/napc/physics/FEC/FEC2012/html/fec12.htm

[5] Chen W. *et al* 2011 *Nucl. Fusion* **51** 063010

[6] Ding X.T. *et al* 2013 *Nucl. Fusion* **53** 043015

[7] Zhong W.L. *et al* 2013 Observation of ELM-free H-mode in the HL-2A tokamak *Nucl. Fusion* at press

[8] Cheng J. *et al* 2012 *Proc. 24th Fusion Energy Conf. (San Diego, CA, 2012)* (Vienna: IAEA) EX/P7-24

www-naweb.iaea.org/napc/physics/FEC/FEC2012/html/fec12.htm

[9] Xu M. *et al* 2012 *Phys. Rev. Lett.* **108** 245001

[10] Xu M. *et al* 2012 *Proc. 24th Fusion Energy Conf. (San Diego, CA, 2012)* (Vienna: IAEA) EX/7-2Rb

www-naweb.iaea.org/napc/physics/FEC/FEC2012/html/fec12.htm

[11] Cheng J. *et al* 2013 *Nucl. Fusion* at press

[12] Zhao K.J. *et al* 2013 *Nucl. Fusion* **53** 083011

[13] ITER Physics Basis 1999 *Nucl. Fusion* **39** 2715

[14] Rapp J. *et al* 2002 *Plasma Phys. Control. Fusion* **44** 639

[15] Lang P.T. *et al* 2003 *Nucl. Fusion* **43** 1110

[16] Evans T.E. *et al* 2004 *Phys. Rev. Lett.* **92** 235003

[17] Schaffer M.J. *et al* 2008 *Nucl. Fusion* **48** 024004

[18] Baylor L.R. *et al* 2013 *Phys. Rev. Lett.* **110** 245001

[19] Duan X.R. *et al* 2010 *Nucl. Fusion* **50** 095011

[20] Duan X.R. *et al* 2012 *IEEE Trans. Plasma Sci.* **40** 673

[21] Xiao W.W. *et al* 2012 *Proc. 24th Fusion Energy Conf. (San Diego, CA, 2012)* (Vienna: IAEA) EX/6-3Ra

www-naweb.iaea.org/napc/physics/FEC/FEC2012/html/fec12.htm

[22] Zou X.L. *et al* 2012 *Proc. 24th Fusion Energy Conf. (San Diego, CA, 2012)* (Vienna: IAEA) PD/P8-08

www-naweb.iaea.org/napc/physics/FEC/FEC2012/html/fec12.htm

[23] Rhee T. *et al* 2012 *Phys. Plasmas* **19** 022505

[24] Fasoli A. *et al* 2007 *Nucl. Fusion* 47 S264

[25] Chen L. *et al* 2007 *Nucl. Fusion* **47** S727

[26] Chen L. *et al* 2008 *Plasma Phys. Control. Fusion* **50** 124001

[27] Chen W. *et al* 2010 *Nucl. Fusion* **50** 084008

[28] Chen W. *et al* 2010 *Phys. Rev. Lett.* **105** 185004

[29] Yu L.M. *et al* 2013 *Nucl. Fusion* **53** 053002

[30] Wang X. *et al* 2010 *Plasma Phys. Control. Fusion* **52** 115005

[31] Macor A. *et al* 2009 *Phys. Rev. Lett.* **102** 155005

[32] Zonca F. *et al* 2007 *Nucl. Fusion* **47** 1588

[33] Deng W. *et al* 2013 Investigation of the role of energetic particle in the driving of long-lived saturated internal mode on HL-2A tokamak *Nucl. Fusion* submitted

[34] Menard E. *et al* 2005 *Nucl. Fusion* **45** 539

[35] Chapman I.T. *et al* 2010 *Nucl. Fusion* **50** 045007
[36] McKee G.R. *et al* 2003 *Phys. Plasmas* **10** 1712
[37] Conway G.D. *et al* 2008 *Plasma Phys. Control. Fusion* **50** 055009
[38] Xu M. *et al* 2009 *Phys. Plasmas* **16** 042312
[39] Xu M. *et al* 2010 *Phys. Plasmas* **17** 032311
[40] Zhao K.J. *et al* 2009 *Nucl. Fusion* **49** 085027
[41] Biskamp D. 2000 *Magnetic Reconnection in Plasmas* (Cambridge: Cambridge University Press)
[42] Kaw P.K., Valeo E.J. and Rutherford P.H. 1979 *Phys. Rev. Lett.* **43** 1398
[43] Diamond P.H. *et al* 2005 *Plasma Phys. Control. Fusion* **47** R35
[44] Boedo J.A. *et al* 2003 *Phys. Plasmas* **10** 1670
[45] Labombard B. *et al* 2002 *Phys. Plasmas* **9** 1300
[46] Antar G.Y. *et al* 2003 *Phys. Plasmas* **10** 3629
[47] Krasheninnikov S.I. and Smolyakov A.I. 2008 *Phys. Plasmas* **15** 055909
[48] Bleuel J. *et al* 2002 *New J. Phys.* **4** 38
[49] Sanchez E. *et al* 2005 *J. Nucl. Mater.* **337** 296
[50] Tynan G. *et al* 2013 *Nucl. Fusion* **53** 073053
[51] Miki K. *et al* 2013 *Nucl. Fusion* **53** 073044